PHYSICAL REVIEW B **83**, 184112 (2011)

Orientational ordering of interstitial atoms and martensite formation in dilute Fe-based solid solutions

A. Udyansky, J. von Pezold, A. Dick, and J. Neugebauer
Max-Planck-Institut für Eisenforschung GmbH, Max-Planck-Strasse 1, D-40237 Düsseldorf, Germany

(Received 11 January 2011; revised manuscript received 29 March 2011; published 20 May 2011)

We study the thermodynamic stability of dilute C, N, O, B, and C+N interstitial distributions in bcc iron, combining parameter-free density functional theory (DFT) in the generalized gradient approximation and microscopic elasticity theory. This scheme allows us to fully capture the long-range elastic impurity-impurity interactions using moderately sized DFT calculations. Employing this approach we compute temperature-concentration phase diagrams including the effects of external pressure, and provide direct insight into the formation mechanisms of martensite. For all investigated impurities, except for B, tetragonal states are predicted to be preferred even at low impurity concentrations. The preference is shown to originate from a thermodynamically driven orientational ordering of the interstitials.

DOI: 10.1103/PhysRevB.83.184112 PACS number(s): 05.50.+q, 64.60.Cn, 61.72.−y, 71.15.Mb

I. INTRODUCTION

Alloying elements significantly affect the structural and mechanical properties of steels. Even low concentrations of interstitials can trigger the martensitic transformation in iron during quenching from the high-temperature, austenitic face-centered phase. The metastable tetragonally distorted body-centered-cubic (bcc) martensite[1–3] has a great strengthening effect on iron and underlies technologically important properties of steels, such as corrosion resistance, fracture toughness, high mechanical damping, shape memory effect, superelasticity, and superplasticity.[4]

The tetragonality of the martensite lattice is a direct consequence of the preferential occupation of one of the three possible octahedral sublattices by impurities (Fig. 1). The occurrence of ordered phases has been attributed to a homogeneous diffusionless deformation (Bain's transformation)[5,6] from fcc austenite to bcc ferrite, during which the impurity atoms occupying the octahedral interstitial sites of the fcc lattice fall into only one interstitial sublattice of the bcc phase and thus cause the tetragonal distortions. While the formation of such tetragonal states is well established for high impurity concentrations [>0.6 wt % for Fe-C (Ref. 7) and > 0.75 wt % for Fe-N (Ref. 8)], only one experimental study reports the formation of the tetragonal Fe-C martensite[9] at low impurity concentration (0.18 wt %). Zener[10] suggested a "self-induced preferential distribution" of impurity atoms on one octahedral subcell in bcc Fe driven by an elastic (strain-induced) interaction between them. Based on this idea, Kurdjumov and Khachaturyan[11–13] deduced the transition from an ordered tetragonal state to a disordered cubic phase, using the method of static concentration waves[13] and microscopic elasticity theory (MET),[13–16] which takes into account the discrete nature and elastic anisotropy of crystal lattices. The MET is formulated in reciprocal space and *a priori* has no limitations on the interaction radius. It thus naturally takes into account the long-range strain-induced interactions between point defects in an alloy matrix. The order-disorder transition of dilute Fe-C solid solutions at room temperature has been predicted within the framework of the MET,[10,12,17–20] which describes the strain-induced interaction only. However, it has been subsequently shown[13,21] that for an accurate description of the martensitic transformation, also chemical C-C interactions have to be considered in addition to the elastic interaction.

We recently demonstrated[22] the efficiency of combining atomistic simulations with MET for studying martensitic stability limits in a dilute Fe-C solid solution. The employed approach allowed for a consistent description of the strain-induced and chemical interaction of C impurities with all parameters determined using atomistic simulations exclusively. Nevertheless, atomistic methods, based on semiempirical approaches, such as the embedded atom method used in that study, are restricted to the availability of reliable interaction potentials. Moreover, magnetic properties, which play a dominant role in Fe-based solid solutions, are difficult to capture at the atomistic level, although some promising approaches[23] in this direction have emerged over the last few years.

In order to overcome the above-mentioned limitations, we use a combination of parameter-free density functional theory (DFT) and MET to capture both the short-range chemical and the long-range elastic interactions in iron-based systems. In particular, we study the formation mechanism of martensites in bcc Fe with low impurity concentrations and predict their stability limits. The technologically important impurities C, N, O, B, as well as the C+N system, which are commonly employed to tune the hardness, deformability, machinability, corrosion resistance, and strength of steels, are used as alloying elements.

Pressure critically affects the propagation of elastic waves and thus the interatomic interactions, as well as the mechanical stability of solid solutions. Therefore, the order-disorder transition was investigated as a function of the external stress state of the systems.

II. METHOD

A. Interatomic interactions

A fundamental understanding of the physics governing the interactions between interstitial atoms in bcc Fe is critical for a correct description of the properties of steels. In order

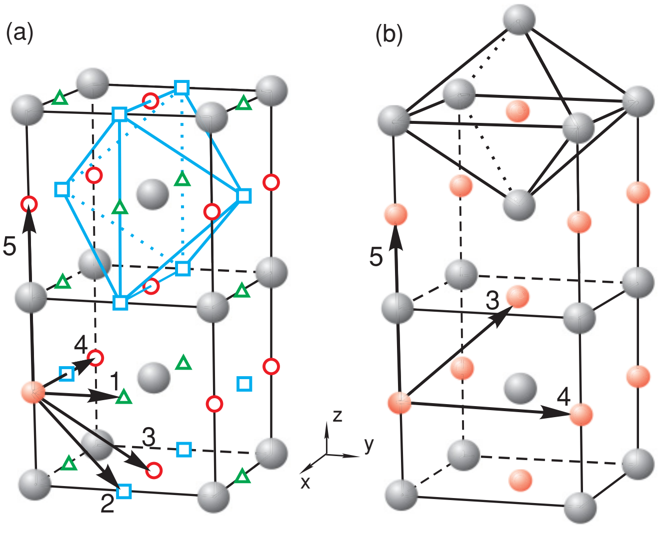

FIG. 1. (Color online) Schematic structure of the bcc lattice, containing (a) three interpenetrating bcc sublattices of octahedral interstices (open circles, triangles, squares) within the Fe host matrix (gray balls), and (b) only one octahedral sublattice occupied by impurity atoms [red (small gray) balls]. Octahedral cages are indicated in either case. Scenario (b) is interpreted as orientational ordering and causes the tetragonal distortions of the Fe host lattice. A fully random distribution of impurities on all three sublattices in (a) results in cubic symmetry. The first five coordination shells for interstitial impurities are indicated by arrows.

to accurately describe impurity-impurity interactions within the Fe matrix, we represent the interaction between two interstitials at positions p and q in two unit cells separated by a translation vector $\mathbf{R}$ in matrix form $\|V_{pq}^{\mathrm{tot}}(\mathbf{R})\|$.[13] In such a matrix, the diagonal elements describe the interaction within each interstitial sublattice (see Fig. 1) and nondiagonal entries correspond to effective cluster interactions between atoms on different sublattices. The total effective pair interaction is considered as a sum of a chemical part $\|V_{pq}^{\mathrm{ch}}(\mathbf{R})\|$ and a strain-induced part $\|V_{pq}^{\mathrm{si}}(\mathbf{R})\|$, which is mediated by lattice relaxation.

The chemical contribution to the impurity-impurity interaction as a function of the impurity separation $\mathbf{R}$ was obtained by calculating the energy of the system with all atoms constrained to their ideal positions. In particular, the pairwise chemical interaction was determined by

$$V_{pq}^{\mathrm{ch}}(\mathbf{R}) = E_{pq}^{\mathrm{Fe}+2X}(\mathbf{R}) - E^{\mathrm{Fe}} - 2(E^{\mathrm{Fe}+X} - E^{\mathrm{Fe}}), \tag{1}$$

where $E_{pq}^{\mathrm{Fe}+2X}(\mathbf{R})$ and $E^{\mathrm{Fe}+X}$ are the energies of the systems containing two X impurity atoms separated by a distance $\mathbf{R}$ and a single X atom within the Fe matrix, respectively. E^{Fe} is the energy of the Fe matrix. The last term is the energy of injection of an interstitial atom X in the Fe host.

The strain due to the presence of interstitial atoms in the system is described as the elastic response of the lattice to a virtual force field, given by the Kanzaki forces $\mathbf{F}_p(\mathbf{R})$.[14,24] Based on this model, the strain-induced interaction potential between two interstitial atoms at positions p and q in two unit cells separated by a translation vector $\mathbf{R}$ reads in reciprocal space as[13,14]

$$V_{pq}^{\mathrm{si}}(\mathbf{k}) = -\mathbf{F}_p(\mathbf{k})\mathbf{G}(\mathbf{k})\mathbf{F}_q^*(\mathbf{k}) + Q_{pp}\delta_{pq}, \tag{2}$$

where Q_{pp} is the self-interaction correction:

$$Q_{pp} = \frac{1}{N}\sum_{\mathbf{k}} \mathbf{F}_p(\mathbf{k})\mathbf{G}(\mathbf{k})\mathbf{F}_p^*(\mathbf{k}). \tag{3}$$

The summation is carried out over the first Brillouin zone by N $\mathbf{k}$ vectors. $\mathbf{F}_p(\mathbf{k})$ is the Fourier component of the pairwise Kanzaki force $\mathbf{F}_p(\mathbf{R})$, $\mathbf{G}(\mathbf{k}) = \mathbf{D}^{-1}(\mathbf{k})(\mathbf{k} \neq 0)$ is the Fourier component of the lattice Green's function,[25] $\mathbf{D}(\mathbf{k})$ is the dynamical matrix, and δ_{pq} is the Kronecker delta.

We neglect the Kanzaki forces for the third and higher coordination shells of the host lattice surrounding the interstitial atoms. This allows us to obtain an analytic expressions for $\mathbf{F}_p(\mathbf{k})$ in terms of macroscopic material properties only: elastic constants c_{ij}, the lattice constant a_0 of the host matrix in the absence of impurity atoms, as well as the $L_{[100]}$, $L_{[010]}$, and $L_{[001]}$ coefficients (see, e.g., Ref. 26), which describe the concentration dependence of the impurity-induced lattice distortions in the [100], [010], and [001] directions, respectively. The analytic form of $\mathbf{G}(\mathbf{k})$ (Ref. 14) is a function of c_{ij} and a_0 only. Note, that the MET is rigorously defined for interstitial alloys since they can be strictly separated into a metal matrix, described by lattice Green's functions and an impurity subsystem which acts on the host matrix by Kanzaki forces.

B. *Ab initio* calculations

The pairwise chemical interactions between the impurity atoms, as well as the parameters for the long-range strain-induced interactions within the MET, have been obtained from DFT[27,28] calculations. For the description of the electron-ion interactions we have employed Blöchl's projector augmented-wave (PAW) potentials[29] in combination with the Perdew, Burke, and Ernzerhof (PBE)[30] parametrization of the exchange-correlation functional, as implemented in the Vienna *Ab Initio* Simulation Package (VASP).[31–34] The ground-state phase of Fe [ferromagnetic (FM) bcc (Ref. 35) at low temperatures] has been assumed in all calculations. The integration over the first Brillouin zone has been performed using the Methfessel-Paxton scheme[36] of order one.

To ensure accurate values of the derived chemical and elastic interactions, careful convergence tests have been performed with respect to the plane-wave (PW) energy cutoff, the k-point mesh, as well as the supercell size.

A plane-wave energy cutoff of 450 eV was found to allow for convergence with respect to the equilibrium lattice constant [Fig. 2(a)] and the bulk modulus of bcc Fe.

To exclude spurious energy contributions due to interactions of the impurity atoms with their periodic images, we studied the convergence of the pairwise chemical interactions $V^{\mathrm{ch}}(\mathbf{R})$ with respect to the supercell size (Fig. 3). A $4 \times 4 \times 4$ cubic supercell containing 128 Fe host atoms, and two interstitial atoms in octahedral sites (see Fig. 1) has been chosen as a compromise between the accuracy of the calculations and their computational feasibility. The use of a k-point mesh equivalent to the $16 \times 16 \times 16$ Monkhorst-Pack[37] mesh for

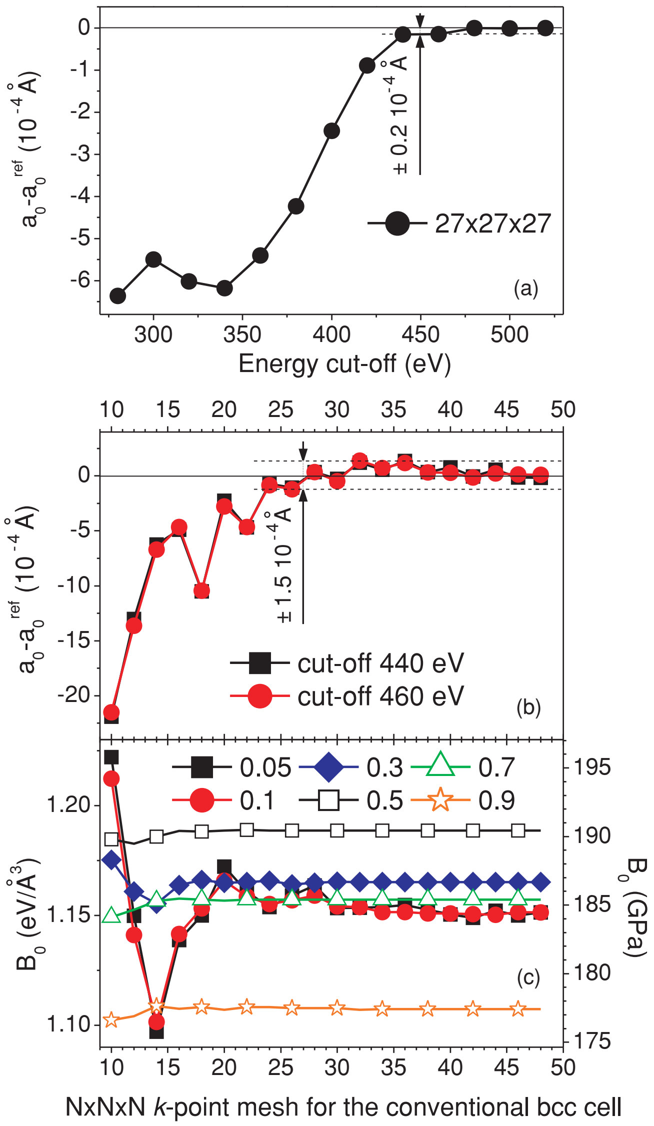

FIG. 2. (Color online) Convergence of the equilibrium lattice constant (a), (b) and bulk modulus (c) of Fe with respect to the cutoff energy (a) and the *k*-point mesh density (b), (c). Squares and circles in (b) correspond to plane-wave cutoff energies of 440 and 460 eV, respectively. a_0^{ref} are the equilibrium lattice constants calculated (a) using a cutoff energy of 520 eV and a 27 × 27 × 27 *k*-point grid, and (b) using a 48 × 48 × 48 *k*-point mesh for either cutoff energy. The maximal error in the calculated lattice constant using a 27 × 27 × 27 *k*-point mesh and a smearing parameter of 0.1 eV is less then 1.5×10^{-4} Å. (c) The different symbols correspond to different electronic temperatures in eV, as marked on the graph.

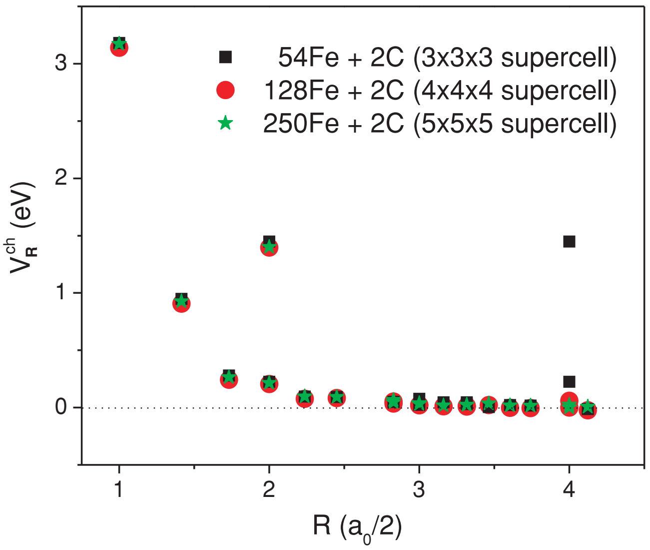

FIG. 3. (Color online) Dependencies of the pairwise chemical contribution to C-C interactions as a function of the C-C separation for supercells of different sizes. Doubling of the supercell of the Fe matrix (from 54 to 128 atoms) dramatically decreases the spurious effect of periodic boundary conditions [note in particular the interatomic distance of $4(a_0/2)$, corresponding to coordination shells 18 and 19].

the conventional bcc cell in conjunction with a smearing parameter of 0.1 eV ensures a convergence of $V^{\text{ch}}(\mathbf{R})$ to within 0.4 meV/atom.

The description of elastic properties tends to require denser *k*-point meshes since the calculation of these quantities implies discontinuous changes in the PW basis set due to variations in the supercell shape. The convergence of the elastic properties (a_0, c_{ij}, B_0) of pure bcc Fe was therefore carefully studied as a function of the *k*-point grid (Figs. 2 and 4) and the smearing parameter σ. As discussed above, the lattice parameter and the elastic constants serve as inputs for the MET-based determination of the long-range elastic interactions. For a reliable application of this approach these parameters therefore need to be well converged. Increasing the smearing parameter σ in the Methfessel-Paxton scheme allows for a more efficient sampling of the Fermi surface, and hence a reduction in the required integration mesh. Our calculations indicate that, although the convergence of the bulk modulus [Fig. 2(c)] and the elastic constants (Fig. 4) with respect to the *k*-point mesh is indeed improved for higher values of σ, the absolute values of the calculated elastic constants are also shifted with increasing σ value. For example, the deviation between the converged result for B_0, as determined using $\sigma = 0.1$ and 0.3 eV is within 1% [Fig. 2(c)], while the deviation between the converged result for c_{44}, obtained for identical smearing parameters, can be as large as 10% (Fig. 4). Such a large variation in c_{44} is critical since its influence on the elastic response of polycrystalline materials was found[38] to be two orders of magnitude larger than that of, e.g., the bulk modulus. To achieve an accuracy of ±5 GPa in the elastic constants (Fig. 4) and a convergence of the lattice constants to within 1.5×10^{-4} Å [Fig. 2(b)], we therefore chose the following parameter set: an energy cutoff of 450 eV and a 27 × 27 × 27 Monkhorst-Pack *k*-point grid per conventional bcc cell in conjunction with a smearing parameter of 0.1 eV. Hence, two different integration meshes were used for the determination of chemical and elastic interaction parameters. We note that, for calculating the elastic properties, a careful choice of the electronic temperature (e.g., $\sigma = 0.3$) may allow a reduction in the *k*-point sampling by a factor of 2–3 times, and a corresponding speed up of the calculations.

The influence of hydrostatic pressure on the energetic and elastic properties of the Fe-based solid solutions was studied using the calculated results for a range of nonequilibrium

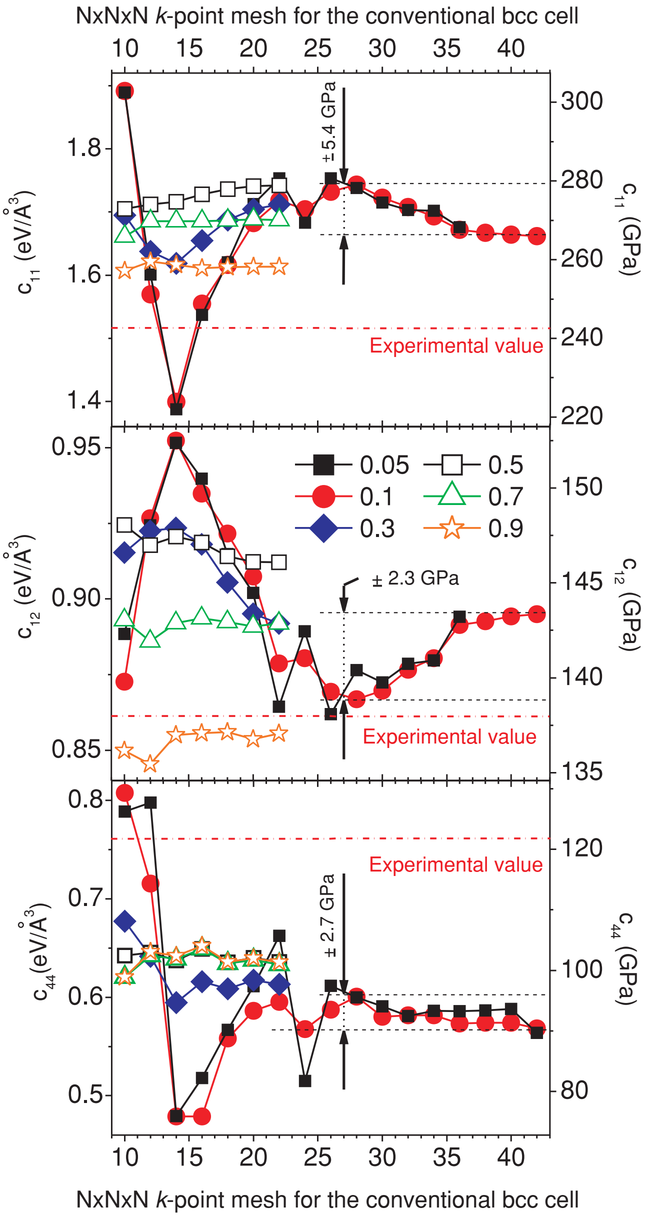

FIG. 4. (Color online) Convergence of the elastic constants of bcc Fe with respect to the number of *k* points. The different symbols correspond to electronic temperatures in eV, as marked on the graph. Experimental measurements (Ref. 39) at 4.2 K are indicated by the dashed-dotted red horizontal line.

volumes V. The transformation of the calculated energies to units of external pressure has been performed using $P(V) = -dE(V)/dV$, where $E(V)$ is provided by the Murnaghan equation of state[40] fitted to the *ab initio* calculated energy-volume data.

III. RESULTS

A. Strain-induced interaction

The equilibrium lattice constant a_0 for the pure Fe matrix was found by a least-squares fit of the total energy as a function of the unit-cell volume, using the Murnaghan equation of state (see Fig. 5 and Table I). The elastic moduli of the cubic crystals have been determined by a well-established approach from the bulk modulus $B = (c_{11} + 2c_{12})/3$, which is directly related to the energy-volume curve, and the two shear moduli, $c_{11} - c_{12}$ (longitudinal strain in the [100] directions – orthorhombic distortions) and c_{44} (shear strain – monoclinic distortions). Both shear moduli are obtained by fitting third-order polynomials to the energy-strain data and extracting the second-order coefficients. The calculated lattice constant and local magnetic moment are in excellent agreement with previous full-potential linearized augmented plane-wave (FLAPW) and PBE data (Table I), indicating that the deviation with respect to experiment is a consequence of the chosen exchange-correlation functional. The experimental elastic properties could be reproduced to within 10%, except for c_{44}, for which a deviation of 25% was obtained. The pressure dependence of the elastic constants is shown in Fig. 6 and their pressure derivatives are listed in Table I. These moduli were calculated at fixed volumes, which correspond to particular external hydrostatic pressures according to the Murnaghan equation of state, as was noted above.

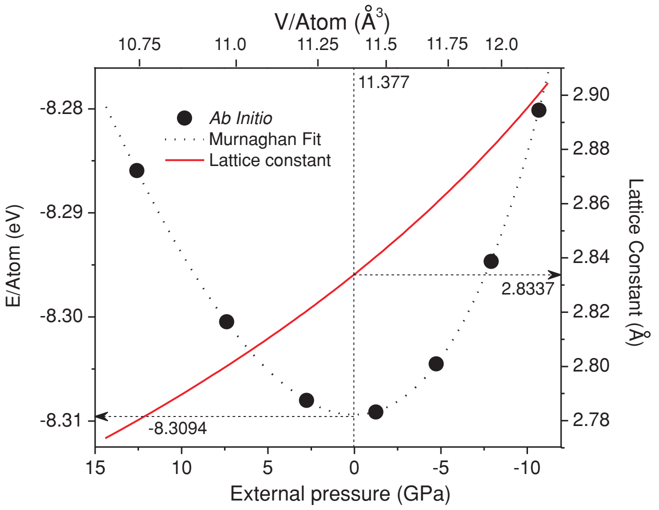

FIG. 5. (Color online) Total energy of bcc Fe (left-hand axis) as a function of the volume per atom (top axis) and the corresponding external pressure (bottom axis). Circles indicate the results of *ab initio* calculations. The dotted line was obtained by a least-square fit to the Murnaghan equation of state $E(V)$. The red (solid) line represents the dependence of the lattice parameter (right-hand axis) on the external pressure determined by differentiating the Murnaghan equation of state.

The numerical measure of the host lattice deformation under an external pressure in the presence of an impurity X is given by

$$L_{[XYZ]}(P) = \frac{1}{a_0^{\mathrm{Fe}}(P)} \frac{a_{[XYZ]}^{\mathrm{Fe}X}(P) - a_0^{\mathrm{Fe}}(P)}{c}, \tag{4}$$

where $a_0^{\mathrm{Fe}}(P)$ and $a_{[XYZ]}^{\mathrm{Fe}X}(P)$ are the lattice parameters of the host Fe matrix and the FeX system under an external pressure P, respectively, and c is the impurity concentration. To evaluate the $L_{[XYZ]}(P)$ parameters we calculated the hydrostatic pressure dependence of the FeX lattice constants along the [100], [010], and [001] directions using a 54-atom Fe supercell with impurity concentrations of 1.818 at. %

TABLE I. Theoretical and experimental lattice constant a_0 (in Å), bulk modulus B_0, elastic constants c_{ij} (in GPa), pressure derivative B_0', and local magnetic moment m_s (in μB) of FM bcc Fe in the absence of external pressure. Theoretical and experimental pressure derivatives dB_0/dP, dc_{ij}/dP of elastic constants are listed in the last three rows. Here PW91 denotes Perdew-Wang exchange-correlation functional, and VWN denotes Vosko-Wilk-Nusair interpolation for the correlation part of the exchange-correlation functional.

	a_0	B_0	B_0'	c_{11}	c_{12}	c_{44}	c'	m_s	Reference
PAW-PBE	2.834	185	5.55	277	140	92	68.5	2.2	This work
PAW-PW91+VWN	2.83	189						2.17	Ref. 34
FLAPW-PW91	2.839	174						2.17	Ref. 41
FLAPW-PBE	2.84	186		279	140	99	69.5	2.17	Ref. 42
PAW-PBE	2.834	174						2.2	Ref. 43
Experiment ($T \sim 0$ K)	2.861	173	5.5(8)	243	138	122	52.5	2.2	Refs. 7, 39, 44, and 45
Pressure derivatives									
PAW-PBE			5.55	7.82	4.42	3.25	1.7		This work
FLAPW-PBE				9.35	3.71	0.62	2.82		Ref. 46
Experiment ($T = 300$ K)			5.29	6.72	4.58	2.59	1.07		Ref. 47

(one impurity atom) and 3.57 at. % (two impurity atoms). The impurity atoms were distributed on a single octahedral sublattice within the supercell so as to maximize their separation. The atomic positions and the shape of the supercell were allowed to relax.

The presence of impurities causes tetragonal distortions of the host lattice for all systems considered (Fig. 7). For each impurity concentration we determined the $L_{[100]}(P)$ and $L_{[001]}(P)$ parameters according to Eq. (4), as indicated by the symbols in Fig. 8. Note that the different impurity concentrations induce different pressure states of the systems. In order to obtain a concentration independent measure of the tetragonality, the pressure dependence of the calculated data was fitted by fourth-order polynomials for either concentration and averaged for each system. It is emphasized that this procedure is not only required to obtain the pressure dependence of $L_{[100]}$ and $L_{[001]}$ but also for the determination of the tetragonality under equilibrium conditions ($P = 0$, see Table II). The agreement of our results with available experimental data is satisfactory, taking into account that the considered impurity distributions may differ from the periodic arrangement assumed here due to imposed periodic boundary conditions.

Having determined all necessary input parameters (a_0, c_{ij}, $L_{[XYZ]}$), the strain-induced interaction $\|V_{pq}^{\mathrm{si}}(\mathbf{k})\|$ was obtained using MET. The eigenvalues $\lambda_\sigma(\mathbf{k})$ of this matrix exhibit a nonanalyticity as shown in Fig. 9. In the close vicinity of the Γ point, the eigenvalues have an undefined value, which is critically dependent on the direction from which the Γ point is approached. Such a behavior is attributed to the long-range character of the strain-induced interactions between impurities and reflects the large Zener anisotropy factor of iron. This principal feature of the strain-induced interaction is the same for all studied impurities and differs only quantitatively.

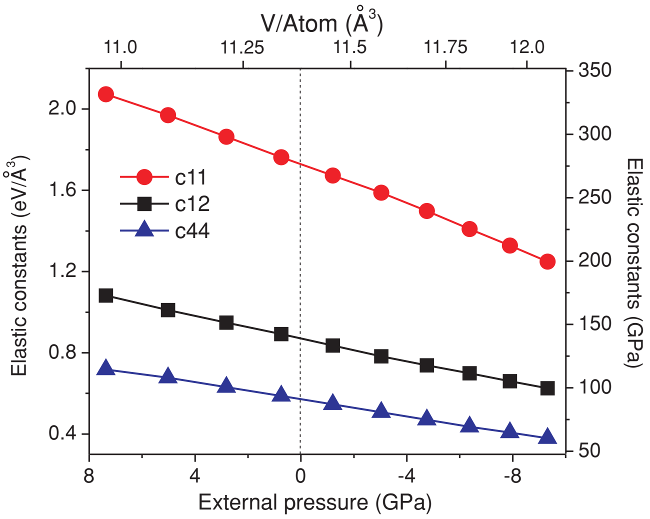

FIG. 6. (Color online) Dependence of the elastic constants of bcc Fe (dots) on the external hydrostatic pressure (bottom axis) and corresponding volume per atom (top axis). The solid lines are fourth-order polynomial fits to the calculated data. Pressure derivatives are listed in Table I.

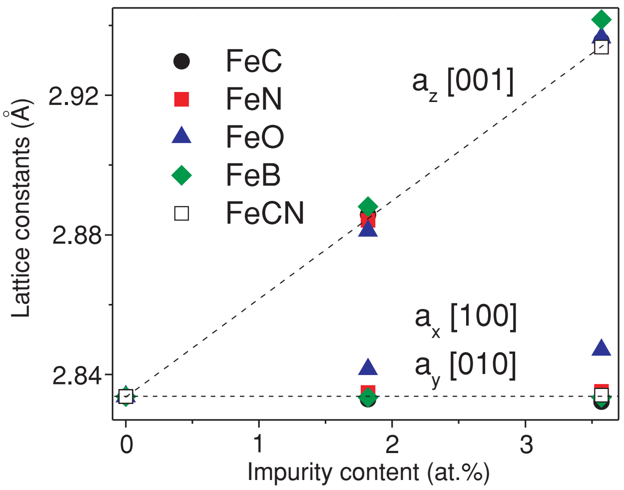

FIG. 7. (Color online) Dependence of the lattice parameters of various Fe-X solid solutions on the impurity concentration under zero external pressure. The dashed lines emphasize the increased tetragonality with increasing concentration and serve as guide to the eye only.

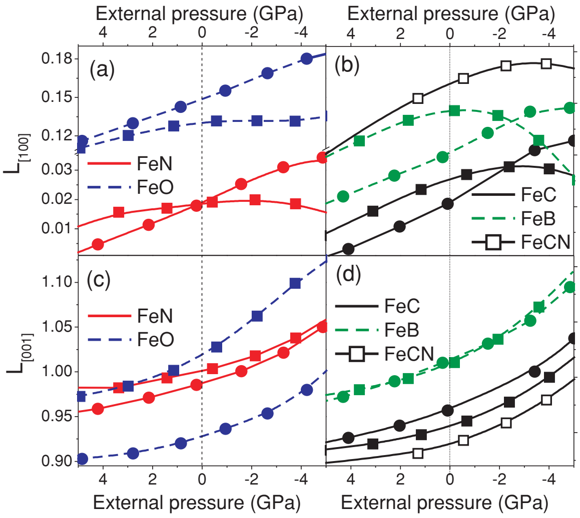

FIG. 8. (Color online) Pressure dependence of $L_{[100]}$ (a), (b) and $L_{[001]}$ (c), (d) for impurity concentrations of 1.818 at. % (circles) and 3.57 at. % (squares). The lines are fourth-order polynomial fits to the calculated data.

B. Chemical interaction

The chemical part of the interaction between impurities was determined *ab initio* by Eq. (1), as shown in Fig. 11(a). For all impurity species considered here the chemical interaction energy is a fast decaying function, which is essentially confined to within the ~7 nearest-neighbor shells. Nonzero interaction energies in shells with higher coordination numbers are attributed to Friedel oscillations and supercell-size effects (see Fig. 3). In order to exclude numerical noise, and taking into account the limited accuracy of our *ab initio* calculations (uncertainty in pairwise interaction parameters of ~50 meV for a supercell consisting of 128 Fe atoms), we focus in the following analysis on the first seven shells. This is equivalent to assuming a cutoff radius of $2.5a_0/2$ (3.55 Å) for the chemical interaction between the impurities. It is noted that despite the obvious effect of periodic boundary conditions on the impurity-impurity interactions in higher coordination shells (e.g., shells 18 and 19—see Fig. 3) in the 3 × 3 × 3 supercell, a comparison with larger supercells shows that this supercell is sufficient to describe the pairwise chemical interactions in the lower coordination shells considered in this study. As for the elastic interactions, the chemical interactions were obtained as a function of the pressure state of the involved systems [$Fe_{128}X_2$, $Fe_{128}X$, and bulk Fe, see Eq. (1)], as determined using the Murnaghan equation of state. External pressure significantly affects the interaction between nearest-neighbor impurities (squares in Fig. 10), while for interactions in all other shells the dependence is weak. In order to include the pressure dependence of the pairwise chemical interactions in the following analysis, *ab initio* determined data points were interpolated by third-order polynomials. As an example, the results for the pairwise interaction between N atoms in the first four neighbor shells are shown in Fig. 10. Similar dependencies were obtained for all impurities considered.

TABLE II. Parameters for the Kanzaki forces obtained *ab initio* at zero external pressure. Parameters based on available experimental data are listed in parentheses.

System	$L_{[100]}$	$L_{[001]}$
FeC	−0.017	1.013
	(−0.09) (Ref. 7)	(0.86) (Ref. 7)
FeN	0.02	0.993
	(−0.07) (Ref. 8)	(0.83) (Ref. 8)
FeO	0.14	0.972
FeB	−0.006	1.064
FeCN	0.00373	0.989

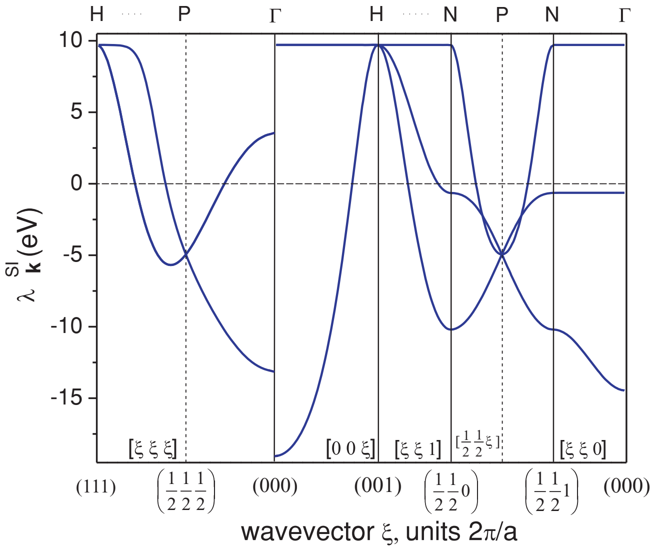

FIG. 9. (Color online) Dispersion curves for the eigenvalues, $\lambda_\sigma(\mathbf{k})$, of the strain-induced interaction matrix of the Fe-C system at zero external pressure.

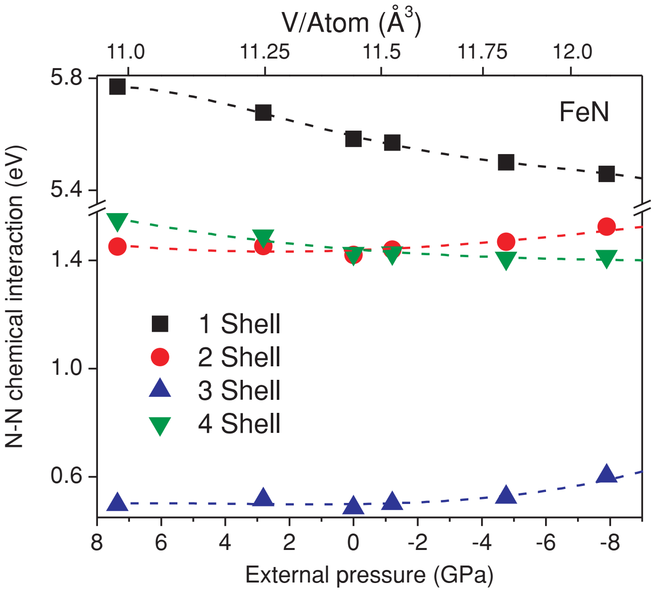

FIG. 10. (Color online) Dependence of the N-N chemical interaction on external pressure (bottom axis) and corresponding volume per atom (top axis). Only the interaction within the first four shells are shown. Symbols indicate *ab initio* results and lines represent the third-order polynomial fits.

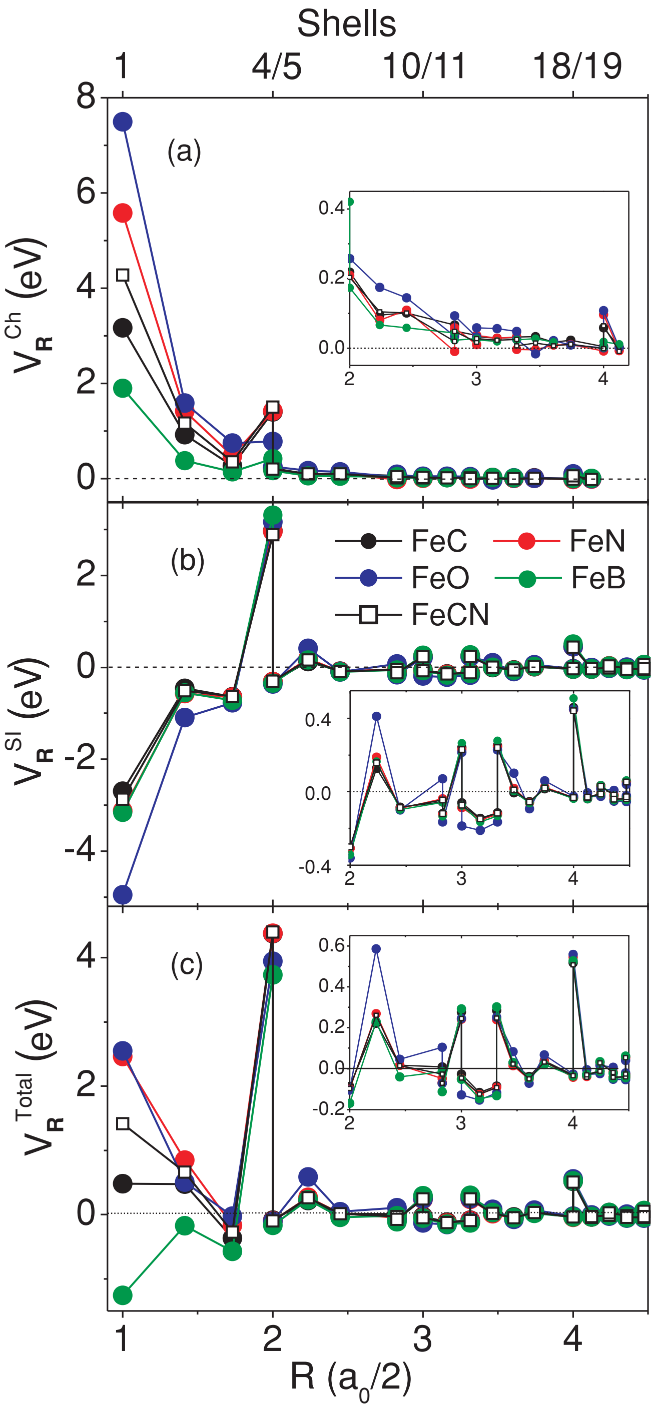

FIG. 11. (Color online) Dependence of pairwise (a) chemical, (b) strain-induced, and (c) total impurity-impurity interactions as a function of the separation distance. The insets magnify the interactions within shells with higher coordination number. The top axis indicates the coordination shells corresponding to the interaction radii.

C. Total interaction

In order to compare the general features of the strain-induced interactions obtained within the MET [in reciprocal space—Eq. (2)] and the chemical interactions directly derived by the *ab initio* calculations [in real space—Eq. (1)] we Fourier transform the strain-induced interaction into real space:

$$V^{\mathrm{si}}_{pq}(\mathbf{R}) = \frac{1}{N}\sum_{\mathbf{k}} V^{\mathrm{si}}_{pq}(\mathbf{k})e^{i\mathbf{kR}}. \qquad (5)$$

In contrast to the fast decaying chemical interactions [Fig. 11(a)], the strain-induced pair interactions exhibit a long-range oscillatory behavior in real space [Fig. 11(b)], originating from the slow decay of the atomic displacement field, induced by the impurity atoms. We remark that a real-space description of such long-range strain-induced interactions would be challenging, while they are naturally taken into account in a reciprocal-space formulation, such as the MET.

The superposition of chemical and strain-induced interaction energies between C-C, N-N, O-O, and C-N impurities are strongly repulsive in the first two coordination shells and attractive in the third shell. The total pairwise interaction between B-B atoms, on the other hand, is attractive in the first three coordination shells. For impurities separated by a larger distance, however, the character of the interaction is qualitatively similar for all impurities considered and clearly dominated by the strain-induced part (see the insets in Fig. 11). The dominance of the strain-induced interactions justifies the truncation of the chemical interaction beyond the seventh coordination shell, as discussed above.

For the following discussion it is convenient to express the total interaction matrix in Fourier space: $\|V^{\mathrm{tot}}_{pq}(\mathbf{k})\| = \|V^{\mathrm{ch}}_{pq}(\mathbf{k})\| + \|V^{\mathrm{si}}_{pq}(\mathbf{k})\|$. Here $\|V^{\mathrm{ch}}_{pq}(\mathbf{k})\|$ and $\|V^{\mathrm{si}}_{pq}(\mathbf{k})\|$ are the matrices of the strain-induced and chemical contributions to impurity-impurity interactions in reciprocal space, respectively. By diagonalizing the total interaction matrix its eigenvalues $\lambda_\sigma(\mathbf{k})$ are obtained, where the index σ specifies the interstitial sublattice. According to the static concentration wave method,[13] the configurational energy of the most stable phase is defined by the global minimum of $\lambda_\sigma(\mathbf{k})$. Using the interaction matrices based on our *ab initio* calculations for the different impurities, we find the minimal eigenvalue at $\mathbf{k} = 0$ in all cases, which corresponds to an infinite interatomic distance in real space. The global minimum is represented in terms of the following interaction matrix, $\lambda_1(\mathbf{k}=0) = V^{\mathrm{tot}}_{11}(0) + 2V^{\mathrm{tot}}_{12}(0)$ and $\lambda_2(\mathbf{k}=0) = V^{\mathrm{tot}}_{11}(0) - V^{\mathrm{tot}}_{12}(0)$, while $\lambda_3(\mathbf{k}=0)$ is degenerate to $\lambda_1(\mathbf{k}=0)$. The minimum of λ_2 at $\mathbf{k}=0$ corresponds to an ordered structure[13] in which only one octahedral sublattice is occupied by impurity atoms. Such ordering with a well-defined orientation results in tetragonal distortions of the Fe host matrix. The minimum of λ_1 at $\mathbf{k}=0$ corresponds to a disordered phase, where all three interstitial sublattices are occupied with equal probability.

TABLE III. Eigenvalues in eV of the impurity-impurity interaction matrix $\|V^{\mathrm{tot}}_{pq}(\mathbf{k})\|$ at zero external pressure.

System	$\lambda_1(\mathbf{k}=0)$	$\lambda_2(\mathbf{k}=0)$
FeC	1.00	−6.380
FeN	12.390	−9.929
FeO	7.322	−9.357
FeB	−17.411	3.764
FeCN	6.893	−7.953

Depending on whether the global minimum is at $\lambda_1(\mathbf{k}=0)$ or $\lambda_2(\mathbf{k}=0)$, a disordered or ordered state is realized. Applying this criterion, we find for all solid solutions studied here the orientationally ordered, tetragonally distorted state except for the boron impurities (see Table III).

The qualitatively different behavior of B compared to all other impurities can be understood by analyzing the real-space total interactions in the first shells [Fig. 11(c)]. Unlike all other impurity atoms, only B atoms exhibit attractive (negative) interactions in the first two coordination shells. The interaction in the third shell, which corresponds to impurities on the same sublattice (shell 3 in Fig. 1) is attractive for all impurities considered. Therefore, for C-C, N-N, O-O, and C-N, the first attractive (stable) configuration involves interstitials on a single sublattice only. This preferential occupation of a particular sublattice is the fundamental origin of the tetragonal distortion of these solid solutions. In contrast, B-B favors nearest- and next-nearest-neighbor pairs on *different* interstitial sublattices. Thus, the qualitatively different interactions in the first two neighbor coordination shells explains why C, N, O, and C-N can form martensite, while at least in thermodynamic equilibrium this is not possible for B. The predicted thermodynamic instability of a B-induced martensite phase is in line with the absence of any experimental observation[48] of such a phase.

Moreover, the predicted repulsive C-C, N-N, and C-N interactions within the first two coordination shells is consistent with Mössbauer spectroscopy-based investigations (see, e.g., Refs. 49 and 50).

D. Thermodynamics

The configurational free energy of the orientationally ordered structure can be expressed[13] within a mean-field approximation in terms of the eigenvalues $\lambda_1(\mathbf{k}=0)$ and $\lambda_2(\mathbf{k}=0)$ of the total interaction matrix:

$$\begin{aligned}F(c,\eta) = {} & \frac{N}{2}\lambda_1(\mathbf{k}=0)\left(\frac{c}{3}\right)^2 + 3N\lambda_2(\mathbf{k}=0)\left(\frac{c}{3}\right)^2\eta^2 \\ & + k_B T N\left\{2\frac{c}{3}(1-\eta)\ln\left[\frac{c}{3}(1-\eta)\right] + \frac{c}{3}(1+2\eta)\right. \\ & \times \ln\left[\frac{c}{3}(1+2\eta)\right] + 2\left[1-\frac{c}{3}(1-\eta)\right] \\ & \times \ln\left[1-\frac{c}{3}(1-\eta)\right] + \left[1-\frac{c}{3}(1+2\eta)\right] \\ & \left. \times \ln\left[1-\frac{c}{3}(1+2\eta)\right]\right\}. \qquad (6)\end{aligned}$$

Here the first two terms denote the enthalpy of the solid solution and the remaining terms describe the configurational entropy. η is the long-range order (LRO) parameter of the system with $\eta = 1(0)$ for the perfectly ordered (disordered) state, k_B is the Boltzmann constant, and T is the absolute temperature. The concentration c corresponds to the atomic fraction of impurities in the Fe matrix.

The LRO parameter can be easily obtained as a function of temperature (see Fig. 12) by numerically minimizing the free-energy functional Eq. (6) and keeping the impurity concentration fixed. As a direct result, we obtain the critical temperature T_0 at which η abruptly changes from 0 to η_0. The abrupt (discontinuous) change corresponds to a first-order phase transition.

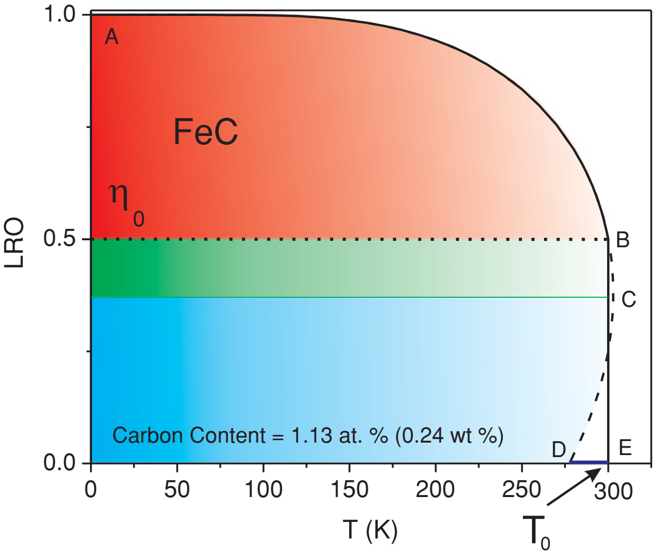

FIG. 12. (Color online) Long-range order parameter as a function of temperature assuming a carbon content of 1.13 at. % in the Fe host matrix. The equilibrium LRO parameter at $T = 300$ K is defined by $\delta F/\delta\eta = 0$ and indicated by the dotted line. The AB region of η values corresponds to the absolute stability of the ordered phase; BC delineates the metastable ordered phase, for which the energy minimum of the ordered phase is higher than the energy minimum of the disordered phase; in the CD region ordered phases are absolutely unstable; DE is the region of metastable stability of the disordered phase. A first-order phase transition occurs at point B at a temperature T_0 corresponding to the critical LRO parameter η_0.

Using this approach the dependence of the order-disorder transition temperature on the impurity concentration can be obtained:

$$T_0 = -\frac{\lambda_2^{\min}(\mathbf{k}=0)c}{k_B}\left\{\ln\frac{[1+2\eta_0][3-c(1-\eta_0)]}{[1-\eta_0][3-c(1-\eta_0)]}\right\}^{-1}. \qquad (7)$$

Here η_0 is the equilibrium LRO parameter defined by $\delta F/\delta\eta|_{\eta=\eta_0} = 0$.

Solving Eq. (7) together with the equilibrium condition $F(c,\eta_0) = F(c,0)$ for ordered and disordered phases, we evaluated the temperature-dependent stability range of the disordered phase, as a function of the impurity concentration (Fig. 13). The disordered state consists of a random distribution of the impurity atoms over all octahedral interstices of the host Fe bcc lattice involving no orientational ordering and tetragonal distortions. All systems for which orientational ordering is predicted behave qualitatively the same. The critical concentrations at which such transition occurs at room temperature are listed in Table IV.

In the predicted phase diagram (Fig. 13) the experimental eutectoid isotherms (1000 K for Fe-C and 865 K for Fe-N) and the solubility limits of C (0.09 at. %/0.02 wt %) and N (0.4 at. %/0.1 wt %) in bcc Fe are indicated by thin lines colored in green and blue, respectively, in order to delineate the concentration regime, in which the order-disorder transition can take place. The N solubility in bcc Fe is considerably higher (by a factor of 4) than that of C and the eutectoid

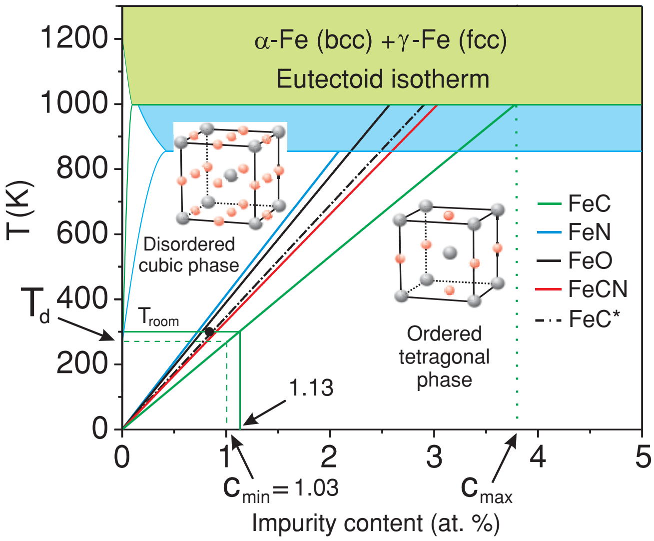

FIG. 13. (Color online) Predicted equilibrium phase diagram of Fe-based solid solutions. The order-disorder transformation temperatures (T_0) as calculated by Eq. (7) are plotted by solid lines. The dot corresponds to the only available experimental data (Ref. 9) for the dilute Fe-C system. Above c_{max} the disordered Fe-C phase is thermodynamically unstable. Below temperature T_d the disorder-order transition is kinetically hindered, due to the slow diffusion of the interstitial C atoms. Thus no martensitic transformation is expected below the corresponding concentration c_{min}. Qualitatively similar arguments hold for the Fe-N, Fe-O, and Fe-C-N systems. The dashed-dotted line represents the Fe-C solid solution as described by *ab initio* determined chemical interactions and a MET-based description of the strain-induced interaction with experimentally obtained input parameters. No ordered, tetragonally distorted phase was found in the low concentration regime of the Fe-B phase diagram.

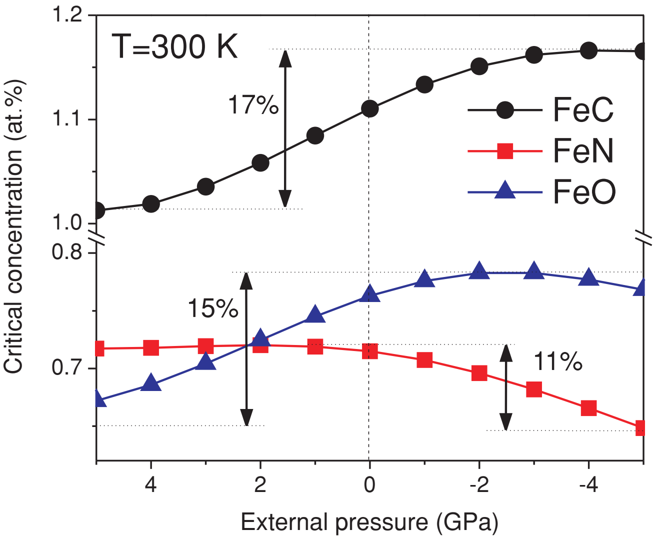

FIG. 14. (Color online) Pressure dependence of the critical concentration of the order-disorder transition at room temperature.

temperature is lower (by 150 K), but qualitatively the relevant part of the Fe-N and Fe-C phase diagram is very similar.

According to Fig. 13, there are two fundamentally different transformation mechanisms giving rise to tetragonal states of Fe-based interstitial solid solutions. Here we discuss them for the example of the Fe-C system. For concentrations above c_{max}, a direct (Bain-type) transformation from austenitic fcc to the ordered (tetragonally deformed) martensite takes place.[5,6] For impurity concentrations below c_{max} the martensitic transformation involves a disordered phase, which has to be ordered by atomistic diffusion during the quenching of the austenitic phase in order to create the tetragonal lattice. Such a rearrangement will be limited by a critical temperature, (T_d), below which the diffusion of the interstitial atoms is kinetically hindered. Using the experimentally observed diffusion barrier of C in bcc Fe of 0.87 eV,[51] T_d is found to be ~270 K. Based on the equilibrium phase diagram (Fig. 13), T_d can be related to a critical carbon concentration c_{min} of 1.01 at. % (0.22 wt %), below which no martensite formation is expected.

TABLE IV. Critical impurity concentration of the order-disorder transition at room temperature under zero external pressure. FeC* corresponds to the solid solution with chemical interactions calculated *ab initio* and strain-induced interactions obtained within the MET with experimentally measured input parameters (see text for details). Experimental data are listed in parentheses.

c_{crit}	FeC	FeN	FeO	FeCN	FeC*
at. %	1.13 (0.84) (Ref. 9)	0.72	0.77	0.9	0.87
wt %	0.24 (0.18) (Ref. 9)	0.18	0.22		0.187

The same arguments also hold for N, O, and C+N impurities in the bcc Fe host matrix. The Fe-N system is the least stable with respect to a order-disorder transformation—it exhibits the smallest concentration-temperature regime corresponding to the stability of the disordered, cubic phase. In other words, our results suggest that N is the strongest martensite stabilizer among the impurities considered in this study. The relative stability of the ordered phase in the presence of the different impurities follows from the relative magnitude of the eigenvalues of the respective interaction matrices (Table III). The entropic contributions to the free energy hence do not significantly influence the stability of the solid solutions considered in this study.

The only available quantitative experimental evidence for an order-disorder transition at room temperature was reported for carbon. A critical C concentration of 0.84 at. % (0.18 wt %) (Ref. 9) (indicated by a dot in Fig. 13) was reported based on x-ray diffraction measurements, which is ~25% off the 1.13 at. % (0.24 wt %), found in this study. The experiment was performed on polycrystalline samples, in which sizable internal stresses are expected due to misfit strains. To estimate how strain affects the critical impurity concentration, we use our computed pressure dependence of the strain-induced (Figs. 5, 6, and 8) and chemical (Fig. 10) interaction parameters. We find a notable change (of up to 17% for C impurities) in the critical concentration at room temperature for hydrostatic pressures between ±5 GPa (Fig. 14). The discrepancy between our results and experimental data may therefore be partly explained by the presence of residual strains in the polycrystalline samples.

A further reason for the discrepancy may be due to the fact that the temperature dependence of the critical concentrations at all external pressures was obtained using our *ab initio* determined 0 K elastic constants of Fe (Table I). In order to analyze the influence of the temperature dependence of the elastic constants on the critical impurity concentration, we repeated our analysis using experimentally determined finite temperature elastic constants.[39,52] At room temperature, the adjusted elastic constants give rise to very modest increases (between 1% for Fe-N and ~7% for Fe-C) in the critical concentrations.

The principal origin of the discrepancy between our results and the experimentally observed critical C concentration is attributed to limitations in the description of the 0 K elastic properties of Fe (Table I) and its solid solutions (Table II) by the exchange-correlation functional used. This becoms evident when replacing the *ab initio* determined input parameters for the MET (a_0, c_{ij}, $L_{[XYZ]}$) by experimental data at $T \sim 0$ K and combining the thus obtained strain-induced interaction terms with the *ab initio* calculated chemical ones. Using this combined experimental and theoretical approach a critical concentration of 0.87 at. % (0.187 wt %) at room temperature under zero external pressure (see the dashed-dotted line in Fig. 13) is found in good agreement with the available experimental value. This fact indicates that a combined approach, involving an *ab initio* determined chemical interaction term and an experimentally informed MET-based description of the strain-induced interaction allows one to overcome deficiencies due to residual limits in present DFT functionals. For such an approach only computationally inexpensive impurity-impurity interactions within a rigid lattice have to be determined *ab initio*.

IV. CONCLUSIONS

We applied a combination of microscopic elasticity theory with parameter-free *ab initio* calculations for the simulation of structural and thermodynamic properties of technologically important Fe-based interstitial solid solutions. Using DFT calculations we obtain the input parameters for the description of the long-ranged interactions between the impurities within the MET. The consistent, *ab initio* based description of strain-induced and chemical interactions allowed us to predict the low impurity concentration part of the Fe-C, Fe-N, Fe-O, Fe-C-N, and Fe-B phase diagrams.

Despite the limited accuracy of the description of the elastic properties of Fe using DFT, our results provide valuable insight into the relative martensite formation propensity of the different systems, given that they have all been treated on an equal footing. In particular, the fundamental driving force for the formation of the tetragonally distorted martensitic phases of bcc Fe-based solid solutions involving interstitials in octahedral interstices was shown to be the repulsive impurity-impurity interaction in the first two coordination shells. Hence, the lack of tetragonally distorted Fe-B solid solutions could be explained in terms of attractive B-B interactions in the first two nearest-neighbor interaction shells. Conversely, the martensite formation in the presence of C, N, O, and C+N impurities originates from a configurational ordering induced by repulsive interactions in these coordinational shells.

Moreover, the predicted phase diagram suggests an explanation for the scarcity of martensitic phases in dilute Fe-based interstitial solid solutions. In particular, at low concentrations a diffusion-based transformation mechanism is proposed. In this regime the quenching of the fcc austenite to bcc ferrite has to be slow enough to allow the diffusional orientational ordering of impurity atoms, which results in the tetragonality of the Fe host matrix. In contrast, during fast quenching, impurity atoms remain randomly distributed within the cubic Fe matrix. This diffusive transformation mechanism is limited by a lower critical temperature (concentration), below which no martensite formation is expected due to the slow kinetics of the impurity rearrangement.

The concentration boundaries derived for the phase diagram (Fig. 13) agree well with established characteristics of steels. For instance, so called mild steels exhibit a low alloying element content (less than ~0.2 wt % or 0.93 at. % for carbon), are malleable, ductile, and weldable (see, e.g., Ref. 53), and are thus suitable for many applications. As the concentration of the alloying element rises, the hardness and stiffness of steels increases, but their plasticity decreases. Such a change in the properties is attributed to the appearance of martensitic inclusions in the ferritic matrix and is in line with our predictions.

The approach developed in this study is general and can be easily extended to other interstitial or substitutional solid solutions with parameters, obtained solely atomistically or in combination with experimentally measured data.

ACKNOWLEDGMENTS

The authors would like to thank V. Bugaev for his invaluable comments and constant support. Moreover, we would like to acknowledge fruitful discussions with M. Friák, X. Sauvage, and Y. Ivanisenko. We would also like to thank A. Duff for critically reading the manuscript. Financial support through the Triple-M–Max-Planck Initiative on Multiscale Materials Modeling of Condensed Matter is gratefully acknowledged.

---

[1] W. L. Fink and E. D. Campbell, Trans. Am. Soc. Steel Treat. **9**, 717 (1926).

[2] N. Seljakov, G. Kurdjumov, and N. Goudsov, Z. Phys. **45**, 384 (1927).

[3] A. Fry, Stahl Eisen **43**, 1271 (1923).

[4] V. A. Lobodyuk and E. I. Estrin, Phys. Usp. **48**, 713 (2005).

[5] E. Bain, AIME **70**, 25 (1924).

[6] G. V. Kurdjumov and G. Sachs, Z. Phys. **64**, 325 (1930).

[7] C. S. Roberts, Trans. AIME **197**, 203 (1953).

[8] T. Bell and W. S. Owen, J. Iron Steel Inst. **205**, 428 (1967).

[9] Liu Xiao, Zhong Fan, Zhang Jinxiu, Zhang Mingxing, Kang Mokuang, and Guo Zhenqi, Phys. Rev. B **52**, 9970 (1995).

[10] C. Zener, Phys. Rev. **74**, 639 (1948).

[11] G. V. Kurdjumov and A. G. Khachaturyan, Metal. Trans. **3**, 1069 (1972).
[12] G. V. Kurdjumov and A. G. Khachaturyan, Acta Metall. **23**, 1077 (1975).
[13] A. G. Khachaturyan, *Theory of Structural Transformations in Solids* (Wiley, New York, 1983).
[14] M. A. Krivoglaz, *X-Ray and Neutron Diffraction in Nonideal Crystals* (Springer, Berlin, 1996).
[15] H. E. Cook and D. de Fontaine, Acta Metall. **17**, 915 (1969).
[16] D. N. Hoffman, Acta Metall. **18**, 819 (1970).
[17] P. G. Winchell and M. Cohen, Trans. Am. Soc. Met. **55**, 347 (1962).
[18] A. G. Khachaturyan and G. A. Shatalov, Fiz. Met. Metalloved. **32**, 5 (1971).
[19] A. A. Smirnov, Theory of Interstitials Alloys (Nauka, Moscow, 1979).
[20] Zhong Fan, Liu Xiao, Zhang Jinxiu, Kang Mokuang, and Guo Zhenqi, Phys. Rev. B **52**, 9979 (1995).
[21] M. S. Blanter and A. G. Khachaturyan, Phys. Status Solidi A **51**, 291 (1979).
[22] A. Udyansky, J. von Pezold, V. N. Bugaev, M. Friák, and J. Neugebauer, Phys. Rev. B **79**, 224112 (2009).
[23] S. L. Dudarev, R. Bullough, and P. M. Derlet, Phys. Rev. Lett. **100**, 135503 (2008).
[24] H. Kanzaki, J. Phys. Chem. Solids **2**, 2436 (1957).
[25] M. Born and K. Huang, *Dynamical Theory of Crystal Lattices* (Clarendon, Oxford, U.K., 1998).
[26] M. S. Blanter and A. G. Khachaturyan, Metall. Trans. A **9**, 753 (1978).
[27] P. Hohenberg and W. Kohn, Phys. Rev. B **136**, 864 (1964).
[28] W. Kohn and L. J. Sham, Phys. Rev. A **140**, 1133 (1965).
[29] P. E. Blochl, Phys. Rev. B **50**, 17953 (1994).
[30] J. P. Perdew, K. Burke, and M. Ernzerhof, Phys. Rev. Lett. **77**, 3865 (1996).
[31] G. Kresse and J. Hafner, Phys. Rev. B **48**, 13115 (1993).
[32] G. Kresse and J. Furthmuller, Phys. Rev. B **54**, 11169 (1996).
[33] G. Kresse and J. Furthmuller, Comput. Mater. Sci. **6**, 15 (1996).
[34] G. Kresse and D. Joubert, Phys. Rev. B **59**, 1758 (1999).
[35] J. M. Leger, C. Loriers-Susse, and B. Vodar, Phys. Rev. B **6**, 4250 (1972).
[36] M. Methfessel and A. T. Paxton, Phys. Rev. B **40**, 3616 (1989).
[37] H. J. Monkhorst and J. D. Pack, Phys. Rev. B **13**, 5188 (1976).
[38] M. Friák, W. A. Counts, D. Raabe, and J. Neugebauer, Phys. Status Solidi B **245**, 2636 (2008).
[39] J. A. Rayne and B. S. Chandrasekhar, Phys. Rev. **122**, 1714 (1961).
[40] F. D. Murnaghan, Proc. Natl. Acad. Sci. USA **30**, 244 (1944).
[41] H. C. Herper, E. Hoffmann, and P. Entel, Phys. Rev. B **60**, 3839 (1999).
[42] G. Y. Guo and H. H. Wang, Chin. J. Phys. **38**, 949 (2000).
[43] D. E. Jiang and E. A. Carter, Phys. Rev. B **70**, 064102 (2004).
[44] J. Zhang and F. Guyot, Phys. Chem. Miner. **26**, 206 (1999).
[45] C. Kittel, *Introduction to Solid State Physics,* 7th ed. (Wiley, New York, 1996).
[46] H. Ma, S. L. Qiu, and P. M. Marcus, Phys. Rev. B **66**, 024113 (2002).
[47] M. W. Guinan and D. Beshers, J. Phys. Chem. Solids **29**, 541 (1968).
[48] H. Bunzel, E. Kreber, and U. Gonser, J. Phys. (Paris) **35**, C6-609 (1974).
[49] A. G. Balanyuk, V. G. Gavriljuk, V. N. Shivanyuk, A. I. Tyshchenko, and J. C. Rawers, Acta Mater. **48**, 3813 (2000).
[50] V. G. Gavriljuk, A. I. Tyshchenko, J. Rawers, and H. Berns, J. Phys. IV (France) **112**, 259 (2003).
[51] C. A. Wert, Phys. Rev. **79**, 601 (1950).
[52] D. J. Dever, J. Appl. Phys. **43**, 3293 (1972).
[53] M. F. Ashby and D. R. H. Jones, *Engineering Materials 2* (Pergamon, Oxford, 1992).